

Elasticity and lattice dynamics of enstatite at high pressure

Dongzhou Zhang,¹ Jennifer M. Jackson,¹ Bin Chen,^{1,2} Wolfgang Sturhahn,¹
Jiyong Zhao,³ Jinyuan Yan,⁴ and Razvan Caracas⁵

Received 18 February 2013; revised 16 July 2013; accepted 22 July 2013; published 27 August 2013.

[1] The behavior of synthetic-powdered ⁵⁷Fe-enriched enstatite (Mg_{0.980}Fe_{0.020(5)})(Mg_{0.760}Fe_{0.240})Si₂O₆ has been explored by X-ray diffraction (XRD) and nuclear resonant inelastic X-ray scattering (NRIXS). The *Pbca*-structured enstatite sample was compressed in fine pressure increments for our independent XRD measurements. One structural transition between 10.1 and 12.2 GPa has been identified from the XRD data. The XRD reflections observed for the high-pressure phase are best matched with space group *P2₁/c*. We combine density functional theory with Mössbauer spectroscopy and NRIXS to understand the local site symmetry of the Fe atoms in our sample. A third-order Birch-Murnaghan (BM3) equation of state fitting gives $K_{T0} = 103 \pm 5$ GPa and $K'_{T0} = 13 \pm 2$ for the *Pbca* phase. At 12 GPa, a BM3 fitting gives $K_{T12} = 220 \pm 10$ GPa with $K'_{T12} = 8 \pm 4$ for the *P2₁/c* phase. NRIXS measurements were performed with in situ XRD up to 17 GPa. The partial phonon density of states (DOS) was derived from the raw NRIXS data, and from the low-energy region of the DOS, the Debye sound velocity was determined. We use the equation of state determined from XRD and Debye sound velocity to compute the isotropic compressional (V_P) and shear (V_S) wave velocities of enstatite at different pressures. Our results help constrain the high-pressure properties of *Pbca*-structured enstatite in the Earth's upper mantle. We find that candidate upper mantle phase assemblages containing *Pbca*-structured enstatite are associated with shear velocity gradients that are higher than the average Earth model PREM but lower than regional studies down to about 250 km depth.

Citation: Zhang, D., J. M. Jackson, B. Chen, W. Sturhahn, J. Zhao, J. Yan, and R. Caracas (2013), Elasticity and lattice dynamics of enstatite at high pressure, *J. Geophys. Res. Solid Earth*, 118, 4071–4082, doi:10.1002/jgrb.50303.

1. Introduction

[2] The upper mantle plays an important role in the Earth's interior, as the interplay between this region and the lithosphere helps drive plate tectonics, which shapes the surface of the Earth. The depth region between 250 and 300 km is of specific interest in this study. In this depth range, two general features from seismic observations have been identified. One feature is the horizontal variation in *S* wave velocities from different seismic models. These models include global average 1-D models (PREM [Dziewonski and

Anderson, 1981] and AK135 [Kennett *et al.*, 1995]) and regional models for the western United States (TNA [Grand and Helmberger, 1984a]), the eastern North American continent (SNA [Grand and Helmberger, 1984a]), the North Atlantic Ocean (ATL [Grand and Helmberger, 1984b]), and the Pacific Ocean (PAC06 [Tan and Helmberger, 2007]). However, little horizontal variation in the *P* wave velocity structure for this depth range has been reported among different models, including the comparison among global average 1-D models (PREM and AK135) and regional models for the tectonically active western United States (mT7 [Chu *et al.*, 2011]) and the tectonically stable eastern North American continent (CR [Chu *et al.*, 2012] and S25 [LeFevre and Helmberger, 1989]). These seismological models serve as important constraints on determining the composition of this region, because the elasticity of stable phase assemblages must be consistent with seismic observations. The other feature of interest in this depth range is the seismic *X* discontinuity, which is a group of seismic reflections located between 240 and 340 km in depth associated with a shear impedance increase of 3–7.5% [Deuss and Woodhouse, 2002; Revenaugh and Jordan, 1991]. The *X* discontinuity is widespread, but not global, and is characterized by a large depth variation [Deuss and Woodhouse, 2002; Revenaugh and Jordan, 1991]. The presence of hydrated phases in the

¹Seismological Laboratory, Division of Geological and Planetary Sciences, California Institute of Technology, Pasadena, California, USA.

²Now at COMPRES Technology Center, Argonne, Illinois, USA.

³Advanced Photon Source, Argonne National Laboratory, Argonne, Illinois, USA.

⁴Advanced Light Source, Lawrence Berkeley National Laboratory, Berkeley, California, USA.

⁵Centre National de la Recherche Scientifique, Université de Lyon, Université Claude Bernard Lyon 1, Ecole Normale Supérieure de Lyon, Lyon, France.

Corresponding author: D. Zhang, Seismological Laboratory, Division of Geological and Planetary Sciences, California Institute of Technology, 1200 E. California Blvd., Pasadena, CA 91125, USA. (dzzhang@caltech.edu)

upper mantle has been invoked to explain the X discontinuity [Revenaugh and Jordan, 1991; Jacobsen et al., 2010]. However, the X discontinuity has been reported in regions corresponding to the underside of subducted slabs, where hydrated phases are unlikely to be present [Woodland and Angel, 1997; Woodland, 1998].

[3] $(\text{Mg,Fe})_2\text{Si}_2\text{O}_6$ enstatite is the second most abundant mineral in peridotite [Ringwood, 1991; Frost, 2008], containing about 10 to 15% $\text{Fe}_2\text{Si}_2\text{O}_6$, and is one of the three most abundant components in compositional models of the deep upper mantle [Bass and Anderson, 1984; Irifune and Ringwood, 1987; Ringwood, 1991]. The elasticity of orthoenstatite (OEN) has been used to construct petrological models and compare to mantle seismic velocity structures [e.g., Bass and Anderson, 1984; Duffy and Anderson, 1989], and the orthoenstatite (OEN, space group *Pbca*) to high-pressure clinoenstatite (HP-CEN, space group *C2/c*) transition has been suggested to explain the X discontinuity for several reasons. The OEN to HP-CEN transition has a suitable P-T range for the X discontinuity (~ 8.5 – 9.5 GPa along a 1400°C adiabat) [Woodland and Angel, 1997; Woodland, 1998; Kung et al., 2005; Akashi et al., 2009]. Enstatite's abundance in proposed compositional models can explain the existence of X discontinuity in the underside region of subducted slabs [Woodland and Angel, 1997; Woodland, 1998]. The OEN to HP-CEN/majorite-garnet multivariant transition occurs over a large depth interval and is unlikely to produce a sharp seismic discontinuity, thus potentially explaining the wide variability of the X discontinuity [Woodland and Angel, 1997; Woodland, 1998]. Further, recent studies on the pressure-induced transitions of OEN have provided new information regarding the high-pressure symmetry of enstatite [Zhang et al., 2011; Jahn, 2008; Zhang et al., 2012]. Though multianvil experiments have shown that $\text{Mg}_2\text{Si}_2\text{O}_6$ HP-CEN phase is the stable phase at 14 GPa and 1000°C [Kung et al., 2004], a high-pressure study on the vibrational properties of iron-bearing enstatite is still lacking. A better understanding of the high-pressure elastic properties of enstatite with a composition similar to that inferred from petrological observations is needed to make more conclusive statements linking upper mantle seismic structures with the presence of enstatite.

[4] In this study, we present measurements of the elastic properties and lattice dynamics of $(\text{Mg,Fe})_2\text{Si}_2\text{O}_6$ enstatite using X-ray diffraction (XRD) and nuclear resonant inelastic X-ray scattering (NRIXS). XRD has been used in the past to determine the crystal structure, unit cell volume, and P-V equation of state of enstatite [e.g., Hugh-Jones and Angel, 1994; Angel and Jackson, 2002; Akashi et al., 2009]. NRIXS provides information concerning the lattice dynamics of a phase [Sturhahn, 2004] and has also been applied to OEN at ambient conditions [Jackson et al., 2009]. Therefore, in comparison with experimental techniques that have also been used to probe the sound velocities of enstatite, such as Brillouin spectroscopy [e.g., Weidner et al., 1978; Duffy and Vaughan, 1988; Jackson et al., 1999, 2004], ultrasonic interferometry [Frisillo and Barsch, 1972; Webb and Jackson, 1993; Flesch et al., 1998; Kung et al., 2004], and impulsive stimulated light scattering [Chai et al., 1997], NRIXS provides additional information via the partial projected phonon density of states (DOS), such as the mean

square displacement of the iron atoms and the average force constant of the iron sublattice [Sturhahn, 2004; Jackson et al., 2009]. Further, we supplement our experimental results from NRIXS with first-principles calculations to understand how the local site symmetry of the iron atoms may affect the DOS of enstatite. Finally, we combine the elastic properties of iron-bearing enstatite determined in this study with past experimental reports on candidate phases to construct shear velocity profiles of likely petrologies in the Earth's upper mantle. We compare these profiles to global and regional seismic studies, as well as to characteristics of the X discontinuity.

2. Methodology

[5] Powdered starting materials of OEN-structured $(\text{Mg},^{57}\text{Fe})_2\text{Si}_2\text{O}_6$ with 13 mol % $^{57}\text{Fe}_2\text{Si}_2\text{O}_6$ (hereafter referred to as En87) were prepared for high-pressure NRIXS experiments. The starting $^{57}\text{Fe}_2\text{Si}_2\text{O}_6$ was 95% ^{57}Fe enriched. The samples in this experiment were taken from the same run charge that was used in a nuclear resonant scattering study at ambient conditions [Jackson et al., 2009] and high pressures [Zhang et al., 2011], where the distribution of Fe in the M1 and M2 sites was determined by synchrotron Mössbauer spectroscopy giving the formula $(\text{Mg}_{0.980}\text{Fe}_{0.020(5)})(\text{Mg}_{0.760}\text{Fe}_{0.240})\text{Si}_2\text{O}_6$ [Zhang et al., 2011]. Two individual diamond anvil cells (DACs) were loaded with En87 for high-pressure XRD and NRIXS measurements. We describe the DAC preparations, experimental details, and first-principles calculations below.

2.1. X-Ray Diffraction

[6] For the XRD measurements, one symmetric DAC was used. Two type-I diamonds with culets $300\ \mu\text{m}$ in diameter were mounted and aligned to form the anvils. A Re gasket was preindented to $\sim 50\ \mu\text{m}$ thick, and a $125\ \mu\text{m}$ diameter hole was drilled in the center of the preindention using an electrical discharge machine. An $\sim 25\ \mu\text{m}$ thick sample ($\sim 30\ \mu\text{m}$ in diameter) was first compacted out of the powder and then loaded into the gasket hole with two ruby spheres ($\sim 10\ \mu\text{m}$ in diameter) surrounding the sample. The DAC was then Ne gas loaded [Rivers et al., 2008]. After gas loading, the diameter of the sample chamber shrank to $\sim 55\ \mu\text{m}$. The ruby spheres were used to determine the pressure in the sample chamber below 4.6 GPa [Mao et al., 1986], where Ne is in the liquid state [Shimizu et al., 2005]. We estimate the uncertainty in pressure determined using the ruby fluorescence method by computing the standard deviation of the pressure given by the different rubies in the sample chamber before and after each XRD measurement. At pressures above 4.6 GPa, Ne crystallizes and in situ Ne volumes were used to determine the pressure via the Ne equation of state [Dewaele et al., 2008]. As the X-ray sampled enstatite and Ne at the same location, using Ne as a pressure gauge reduced the influence of potential pressure gradients in the sample chamber [Boehler, 2000]. Based on the positions of Ne (111) and (200) diffraction peaks, we estimate the Ne pressure uncertainty to be 0.1 to 0.2 GPa from 5.1 to 19.1 GPa (Table 1).

[7] The XRD measurements were carried out at beamline 12.2.2 of the Advanced Light Source (ALS) at Lawrence Berkeley National Laboratory. The energy (30 keV) and

Table 1. Unit Cell Volumes of the OEN Phase (*Pbca*) and the HP Phase (*P2₁/c*) as a Function of Pressure at Room Temperature Determined From the XRD Data Refinements Using the Reflections Shown in Figure 1a^a

OEN		HP	
Pressure (GPa)	Volume (Å ³)	Pressure (GPa)	Volume (Å ³)
0	836(3)	10.1(1)	773(2)
3.0(2)	816(2)	10.4(1)	773(2)
3.5(2)	811(2)	10.8(2)	772(2)
4.5(3)	807(2)	11.2(2)	770(2)
4.6(4)	806(2)	11.7(1)	768(2)
5.1(1)	805(2)	12.2(1)	767(2)
5.5(1)	802(2)	12.7(1)	765(2)
5.7(1)	800(2)	13.2(1)	762(2)
6.2(1)	799(2)	14.0(1)	760(2)
6.7(1)	797(2)	14.5(1)	757(2)
7.1(1)	794(2)	15.0(1)	757(2)
8.3(1)	788(2)	15.6(1)	755(2)
8.6(1)	788(2)	16.2(1)	753(2)
9.0(1)	785(2)	16.7(2)	752(2)
9.3(1)	785(2)	18.2(2)	748(2)
9.5(1)	784(2)	19.1(1)	746(2)
9.9(1)	783(2)	—	—
10.1(1)	782(2)	—	—
10.4(1)	782(2)	—	—
10.8(2)	780(2)	—	—
11.2(2)	779(3)	—	—
11.7(1)	776(4)	—	—
12.2(1)	774(3)	—	—

^aPressures were determined using the ruby fluorescence method [Mao et al., 1986] (below 4.6 GPa), and from the Ne unit cell volume using the BM3 EOS from Dewaele et al. [2008] (above 4.6 GPa). For pressure determination, Ne (111) and (200) peaks were used. Values in parentheses indicate the uncertainty in the last significant digit.

resolution (1 eV) of the X-rays were determined by a high heat load monochromator, and a focus area of 10 μm × 20 μm (full width at half maximum) was achieved by a Kirkpatrick-Baez mirror system and cleanup slits. A high-resolution mar345 Image Plate Detector System located in the downstream direction of the DAC with a distance of about 0.5 m, was used to collect the XRD patterns. A LaB₆ standard sample was used to calibrate the sample to image plate distance and correct the tilting of the image plate. The diffraction images were integrated into angular-resolved chi files using Fit2D [Hammersley et al., 1996] (Figure 1a). Diffraction peaks in the 2θ range between 7 and 12° can be indexed with enstatite peaks. We used the peaks in this 2θ range to fit the unit cell volume of En87 (labeled in Figure 1a), as this range provided enough peaks for volume refinement, avoided the interference of peaks from other materials such as Ne, and had a relatively flat background. The cleanup slits reduced, but did not eliminate, the influence of X-ray intensity in the tails of the focus area. This effect combined with Re's relatively strong atomic scattering factor [Henke et al., 1993] thus leads to some contribution of the Re gasket to the XRD patterns (Figure 1a). Diffraction peaks in the angular-resolved chi files were fit to a Gaussian shape, and their central position and full width at half maximum served as the input of the unit cell volume and associated uncertainty, respectively. The unit cell volume of the sample was refined using UnitCell [Holland and Redfern, 1997]. In most cases, the volume uncertainty was estimated to be 3% of the unit cell volume, which is larger than the 2σ errors provided by

UnitCell. To determine the best fit equations of state (EOS), the P-V data sets were analyzed using the EOS-FIT (V5.2) least squares package [Angel, 2000] (Figures 2 and 3).

2.2. Nuclear Resonant Inelastic X-Ray Scattering

[8] For the nuclear resonant inelastic X-ray scattering measurements (NRIXS), a panoramic DAC with three large radial openings separated by 120° around the sample was used, so as to increase the detection area and therefore the signal. The panoramic DAC was modified with a 90° opening and a cubic boron nitride backing plate on the downstream side, thus maximizing the range of available diffraction angles for in situ XRD. Similar to the DAC prepared for XRD measurements, two type-I diamonds with culets 300 μm in diameter were mounted and aligned to form the anvils. A Be gasket was used to decrease X-ray absorption in the radial direction. The gasket was preindented to ~50 μm thick, and a 125 μm diameter hole was

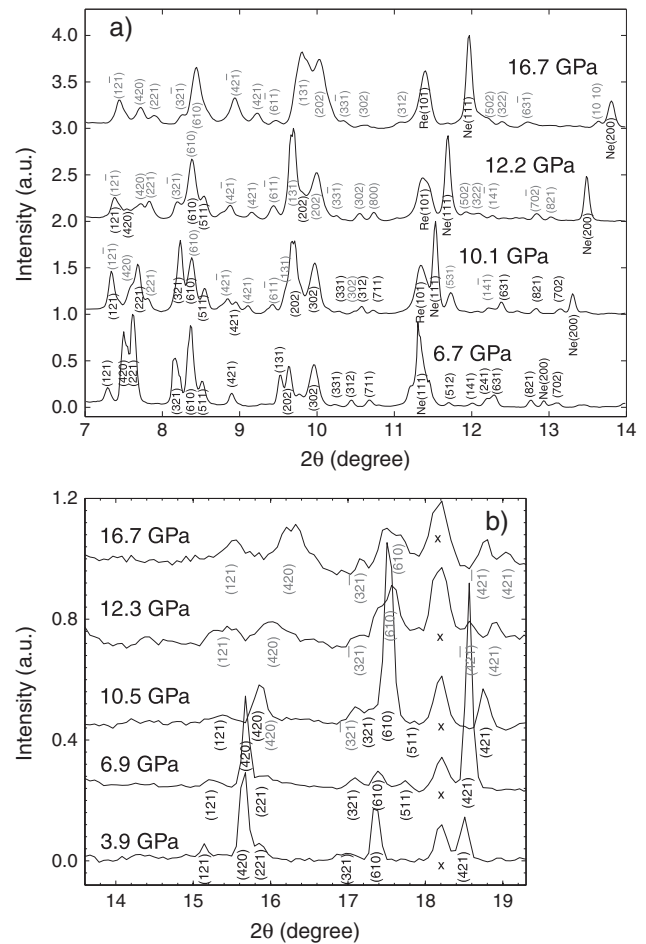


Figure 1. (a) Select XRD patterns at different pressures taken at beamline 12.2.2 of the ALS ($E = 30$ keV). The hkl indices for the OEN phase (*Pbca*, black) and HP phase (*P2₁/c*, gray) are labeled near each peak. Ne and Re peaks are also labeled. (b) Select in situ XRD patterns taken at beamline 3-ID-B of the Advanced Photon Source at the ⁵⁷Fe nuclear resonance energy of 14.4125 keV. Ruby (Al₂O₃) (104) peak (crosses). The background has been subtracted in each pattern.

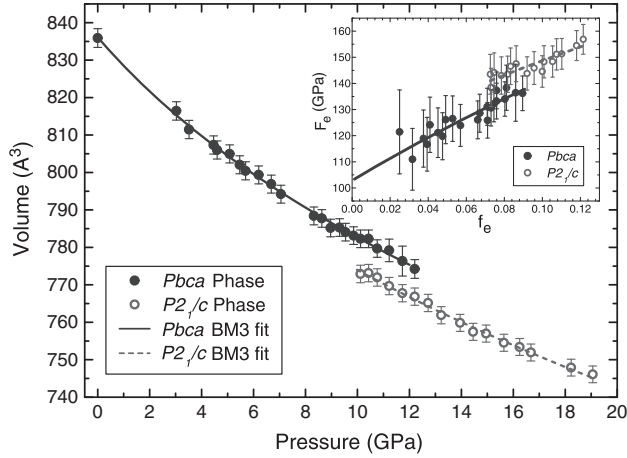


Figure 2. Unit cell volume as a function of pressure for En87 compressed using Ne as a pressure-transmitting medium (Table 1). The best fit third-order Birch-Murnaghan (BM3) equations of state for the two phases are shown as lines (see text for details). Normalized pressure (F_e) versus Eulerian finite strain (f_e) for the En87 sample (inset). Lines are calculated from our reported BM3 EOS.

drilled in the center of the preindention using an electrical discharge machine. The gasket hole was then filled with amorphous boron epoxy to hold the pressure and ensure that the sample maintained a relatively large thickness with increasing pressure. We mechanically drilled an ~ 50 μm diameter hole into the epoxy insert and loaded an ~ 25 μm thick sample (~ 30 μm in diameter, compacted out of the powder) into it. Neon was loaded into the sample chamber of the DAC at the GeoSoilEnviro Center for Advanced Radiation Sources (GSECARS) at the APS [Rivers *et al.*, 2008]. Two ruby spheres (~ 10 μm in diameter) were placed around the En87 sample to monitor the pressure in the sample chamber [Mao *et al.*, 1986], as Ne diffraction peaks were not visible in the sampled 2θ range (Figure 1b).

[9] NRIXS experiments were performed at sector 3-ID-B of the Advanced Photon Source at Argonne National Laboratory. The energy bandwidth of the incident X-rays determines the resolution of the phonon spectra. The X-rays were prepared with bandwidths of 1 meV using a multiple-crystal Bragg reflection monochromator [Toellner, 2000]. A Kirkpatrick-Baez mirror system was used to obtain a focal spot size of $\sim 10 \times 10$ μm^2 at the full width at half maximum [Zhao *et al.*, 2004]. The storage ring was operated in low-emittance top-up mode with 24 bunches that were separated by 153 ns. For each spectrum, the monochromator was tuned from -75 to $+90$ meV around the nuclear resonance energy of ^{57}Fe (14.4125 keV), with a step size of 0.25 meV and a collection time of 5 s per energy step (Figure 4a). The radiation emitted from the sample was observed with four avalanche photodiode detectors. Three detectors were placed around and close to the sample (~ 2 mm away) to collect the incoherent inelastic scattered photons, and the fourth detector was placed downstream (~ 100 cm) in the forward scattering direction, in order to obtain the resolution function independently. The counting rates were low due to the small thickness (in order to achieve pressure) and low ^{57}Fe concentration. Therefore, ~ 10 spectra per pressure were

collected, and the average total counting rate in the highest Stokes peak was ~ 2.2 c/s. In situ X-ray diffraction patterns ($E = 14.4125$ keV and $\lambda = 0.86025$ \AA) were collected at sector 3-ID-B before and after each NRIXS compression point to determine the unit cell volume of the enstatite sample (Figure 1b). We use these volumes to compute the pressure via the best fit BM3 EOS determined from our independent XRD measurements at the ALS (see section 3.1). We did not observe any indication of sample amorphization over the compression range investigated here. The NRIXS data were analyzed using the PHOENIX software package, and a quasi-harmonic model was used to extract the partial phonon density of states (Figure 4b) from the measured raw NRIXS spectra [Sturhahn, 2000].

2.3. First-Principles Calculations

[10] We employ density functional theory (DFT) [Hohenberg and Kohn, 1964; Kohn and Sham, 1965] and density functional perturbation theory [Baroni *et al.*, 1987, 2001; Gonze and Vigneron, 1989; Gonze *et al.*, 1992, 2005] to compute the phonon density of states of $\text{Mg}_2\text{Si}_2\text{O}_6$ OEN. We employ Troullier-Martins-type pseudopotentials [Troullier and Martins, 1991] generated with the Fritz Haber Institute code [Fuchs and Scheffler, 1999], and the generalized gradient approximation in the Perdew-Burke-Ernzerhof formulation [Perdew *et al.*, 1996]. All the calculations are static ($T = 0$ K), and the phonons and DOS are computed in the quasi-harmonic approximation. We fully relax the crystal structure of OEN, minimizing both the residual interatomic forces and the residual nonhydrostatic stresses. We use a $1 \times 2 \times 4$ special grid of high-symmetry \mathbf{k} points [Monkhorst and Pack, 1976] and a cutoff for the plane wave kinetic energy of 34 hartrees (1 Ha = 27.2116 eV). These parameters ensure an accuracy of the calculations better than 1 mHa in energy. We compute the phonons in the Brillouin zone center at ambient pressure. The phonon density of states is built as a summation of the phonon band dispersion, which, in turn, is obtained using Fourier trans-

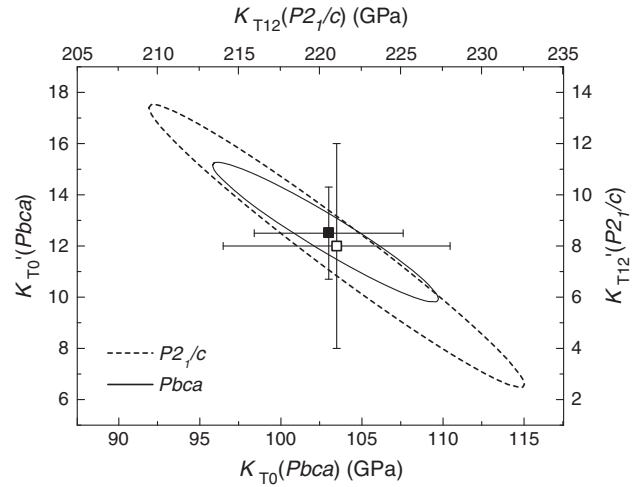


Figure 3. Confidence ellipses in K_T and K'_T for the fit of the BM3 EOS to the En87 P-V data (see text). $PbcA$ (solid square and line). $P2_1/c$ (open square and dashed line). Error bars are given at levels of 1σ . The 68% confidence ellipses are calculated for 2 degrees of freedom [Angel, 2000].

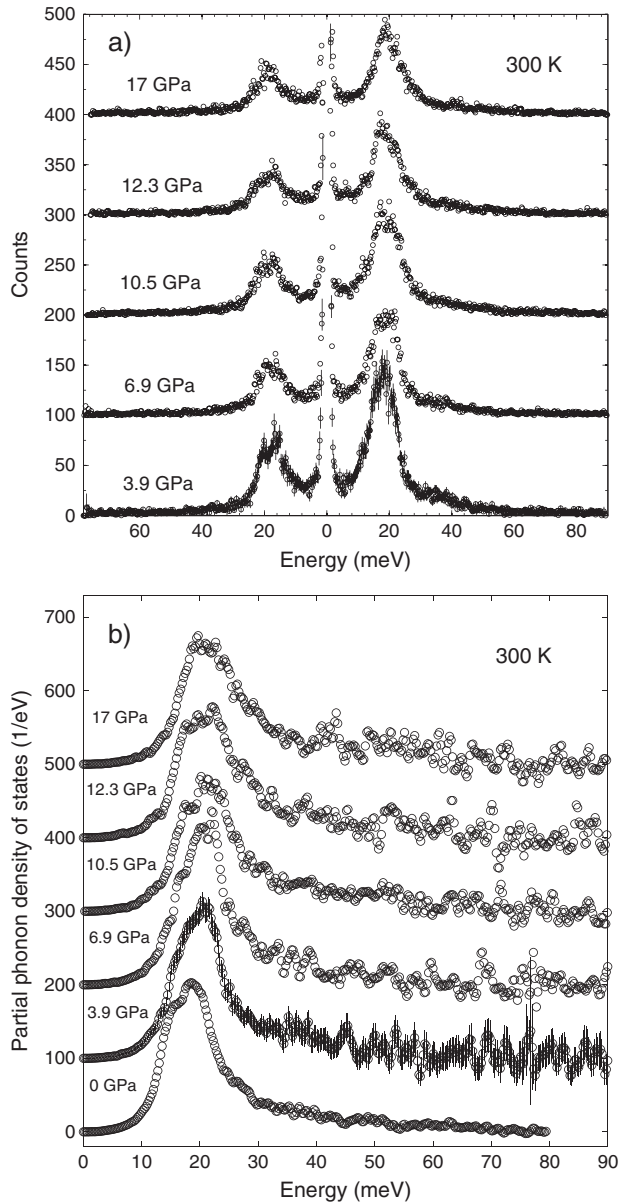


Figure 4. (a) Select NRIXS spectra of En87. Data are shifted vertically. The errors for 6.9, 10.5, 12.3, and 17 GPa are similar to the error of 3.9 GPa but are not plotted for clarity. (b) Partial projected phonon density of states of En87 at different pressures. Each spectrum is offset by 100 units in the vertical direction. Error bars for the ambient pressure data [Jackson *et al.*, 2009] are less than the size of the symbol. Errors for the high-pressure data are similar to those of the 3.9 GPa data.

form techniques of the interatomic force constants matrix at Gamma [Gonze *et al.*, 1992; Baroni *et al.*, 2001].

[11] The DFT calculations are performed on pure $\text{Mg}_2\text{Si}_2\text{O}_6$ compositions. Fe can enter the pyroxene structure on the M1 and/or M2 sites. Once the interatomic force constants matrix is computed for $\text{Mg}_2\text{Si}_2\text{O}_6$, we only alter the mass of the atom on the M1 or M2 site corresponding to the desired amount of iron on that particular position. This is a standard procedure employed for studying isotope partitioning [Schauble, 2004]. We assign the altered mass to be

consistent with the composition of our sample studied by NRIXS. Thus, 25% Fe on either M1 or M2 site in substitution to Mg yields a mass of 32.190. Using the new masses, we recompute the dynamical matrices and reconstruct the phonon density of states (Figure 5). The procedure ensures a first-order approximation of the effect of iron on the total and Fe partial phonon density of states. It has a relatively reduced computational cost and also presents the advantage of preserving the lattice symmetry.

3. Results

3.1. X-Ray Diffraction

[12] We use our results from XRD measurements at the ALS (section 2.1) to determine the pressure-volume equation of state and to monitor the change of crystal symmetry of enstatite. Pressures are determined using the ruby fluorescence method [Mao *et al.*, 1986] (below 4.6 GPa where Ne is in the liquid state) and from the Ne unit cell volume using the BM3 EOS determined from Dewaele *et al.* [2008] (above 4.6 GPa). The pressures determined from each gauge agree up to 15 GPa and then diverge. From the diffraction patterns, one structural transition can be identified between 10.1 and 12.2 GPa. This transition pressure is consistent with previous experimental observations using synchrotron Mössbauer spectroscopy [Zhang *et al.*, 2011], XRD [Kung *et al.*, 2004; Zhang *et al.*, 2012], ultrasonic interferometry [Kung *et al.*, 2004], and theoretical calculations [Jahn, 2008]. Below 10.1 GPa, the diffraction peaks in the 2θ range between 7° and 12° can be indexed with *Pbca* symmetry. At pressures higher than 10.1 GPa, peaks from a new phase emerge in the XRD patterns, and at pressures higher than 12.2 GPa, the diffraction peaks indicate that the sample is converted to a new phase. In the 2θ range between 7° and 12° , the diffraction peaks can be indexed using a monoclinic structure with space group $P2_1/c$ (Figure 1), identified in a recent single-crystal XRD study on $(\text{Mg}_{1.74}\text{Fe}_{0.16}\text{Al}_{0.05}\text{Ca}_{0.04}\text{Cr}_{0.02})(\text{Si}_{1.94}\text{Al}_{0.06})\text{O}_6$ [Zhang *et al.*, 2012]. Therefore, we adopt the $P2_1/c$ structure as the structure for our high-pressure phase. The $P2_1/c$ structure is very similar to the $P2_1ca$ structure, which is a suggested high-pressure symmetry for enstatite based on molecular dynamics simulations [Jahn, 2008]. In our study, there is a density increase of $1.2 \pm 0.5\%$ at 10.1 GPa for the *Pbca* to $P2_1/c$ transition, similar to theoretical results ($\sim 1.3\%$ [Jahn, 2008]) and a recent single-crystal XRD study ($1.9 \pm 0.5\%$ over the pressure range of 12.66 to 14.26 GPa [Zhang *et al.*, 2012]). The density increase for the *Pbca* to $C2/c$ transition in the Mg end-member is reported to be 3 to 4% [Kung *et al.*, 2004].

[13] In order to determine the isothermal bulk modulus (K_T) and the corresponding pressure derivative (K_T') of the En87 sample, third-order Birch-Murnaghan equations of state were used to fit the P-V data sets (Figure 2 and Table 1). The OEN phase (*Pbca*) and the high-pressure phase (hereafter referred to as HP, space group $P2_1/c$) were fit separately. For OEN, we obtained for the zero-pressure unit cell volume (V_0) the same value as our measured value ($836 \pm 3 \text{ \AA}^3$) and a zero-pressure bulk modulus (K_{T0}) of $103 \pm 5 \text{ GPa}$, roughly consistent with previous studies on OEN (Table 2) [Hugh-Jones and Angel, 1997; Flesch *et al.*,

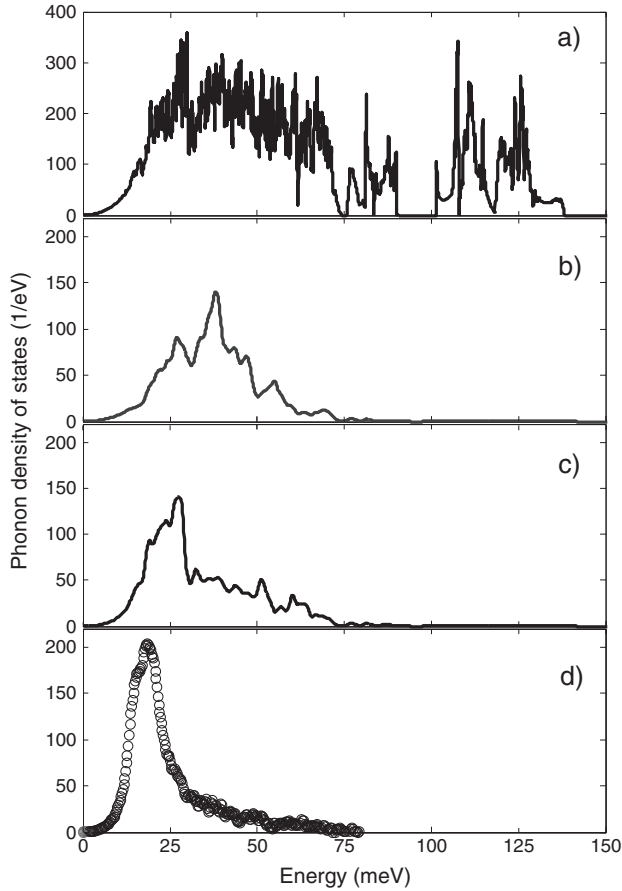


Figure 5. The DFT-calculated phonon DOS (at 0 K) and measured Fe partial projected phonon DOS for OEN at ambient pressure (at 300 K): (a) total phonon DOS of $\text{Mg}_2\text{Si}_2\text{O}_6$ OEN, (b) partial phonon DOS for 25% Mg replaced by Fe on the M1 site, (c) partial phonon DOS for 25% Mg replaced by Fe on the M2 site, and (d) measured Fe partial projected phonon DOS for En87 at 300 K [Jackson *et al.*, 2009].

1998; Angel and Jackson, 2002; Kung *et al.*, 2004]. The disagreement with the study by Chai *et al.* [1997] is likely due to the fact that their sample contained more Al (Table 2). For the pressure derivative of the bulk modulus (K'_{T0}), we obtained 13 ± 2 , consistent with the trend in the normalized pressure (F_e) versus Eulerian finite strain (f_e) (Figure 2). Although this value is higher than previous reports (Table 2), one must recognize the strong correlation between K_{T0} and K'_{T0} (Figure 3).

[14] For the HP phase ($P2_1/c$), the best fit volume at 12 GPa is $767 \pm 3 \text{ \AA}^3$. The best fit bulk modulus of the $P2_1/c$ phase at 12 GPa is 220 ± 10 GPa, significantly higher than the $C2/c$ -structured Mg end-member at the same pressure (168 ± 17 [Shinmei *et al.*, 1999], 177 ± 6 [Angel and Hugh-Jones, 1994], and 186 ± 1 GPa [Kung *et al.*, 2005]). The best fit K'_T at 12 GPa is 8 ± 4 . The 68% confidence ellipses for the K_T and the K'_T fitting are shown in Figure 3. The confidence ellipses show that K_T and K'_T are strongly correlated [Angel, 2000]. We note that our equations of state for both phases should not be extrapolated outside the measured pressure ranges for each phase (see Figure 3).

3.2. Nuclear Resonant Inelastic X-Ray Scattering and First-Principles Calculations

[15] NRIXS measurements provide an independent method to examine the elastic properties of a sample. A quasi-harmonic model was used to extract the partial projected phonon density of states (DOS) (Figure 4) from the measured raw NRIXS spectra [Sturhahn, 2000]. With increasing pressure, the DOS expands and shifts toward higher phonon energies, with subtle changes in shape. From the integration of the DOS, one obtains parameters related to the ^{57}Fe -participating lattice vibrations in the En87 sample: the Lamb-Mössbauer factor, f_{LM} (related to the mean square displacement of the iron atoms); the mean force constant, D_{ave} ; the vibrational free energy per atom, F_{vib} ; the vibrational kinetic energy per atom, E_k ; the vibrational specific heat at constant volume per atom, c_V ; and the vibrational entropy per atom, S_{vib} [Sturhahn, 2000] (Table 3). A subset of these parameters show a minor change in the range of 10.1 to 12.2 GPa, thus indicating some level of sensitivity to the transition.

[16] We compare the ambient phonon DOS from the NRIXS measurement [Jackson *et al.*, 2009] with the phonon density of states calculated from ab initio DFT [Caracas and Gonze, 2010]. For this, we consider three possible cases in the DFT calculations: pure $\text{Mg}_2\text{Si}_2\text{O}_6$, 25% Fe on the M1 site, and 25% Fe on the M2 site. The theoretical total phonon DOS and partial phonon DOS are shown in Figure 5. The measured partial phonon DOS from NRIXS is very similar to the DFT calculation of the partial phonon DOS where the Fe atoms are only in the M2 site (Figures 4 and 5): both have intense phonon peaks around 20 meV, and neither has large intensity around 40 meV. Therefore, the NRIXS data and DFT calculations suggest that the Fe occupation (or more accurate, that the heavier mass element) in the En87 sample is primarily in the M2 site, consistent with synchrotron and conventional Mössbauer studies that 92% of the ^{57}Fe occupies the M2 site [Zhang *et al.*, 2011; Jackson *et al.*, 2009]. Using PHOENIX, we input the various DFT-computed phonon DOSs and calculate the above mentioned parameters at 0 and 300 K for the different considerations of Fe site occupancy (Table 4). Note that the average force constant is independent of temperature. It is not surprising that the parameters are not in good agreement with the experiments, as we consider heavy Mg as a proxy for Fe in our DFT calculations. It is possible to explore the possibility of scaling the DFT-computed DOSs to obtain better agreement. However, this particular exercise would only make sense if the phonon DOSs were computed with Fe, rather than heavy Mg. The absolute values of the free energy may be off significantly, but it is the volume derivative of the free energy that should be compared in this case, and that was not computed by DFT in this study.

[17] By analyzing the low-energy region of the measured partial phonon DOS, one can obtain the Debye sound velocity (V_D) of the sample. The Debye sound velocity is the isotropic sound velocity of the material, obtained from the region in the DOS where the dispersion of the acoustic modes is linear (or the DOS is parabolic) as a function of energy. The energy range that provided the best fit is from 3.7 to 12.2 meV (Figure 6). This range avoids the elastic peak (resolution function) at lower energies [Sturhahn and Jackson, 2007; Jackson

Table 2. Unit Cell Volume, Isothermal Bulk Modulus, and Its Pressure Derivative of Ortho-
enstatite (*Pbca*) at Room Pressure and Temperature From Different Experimental Studies^a

	En100 ^b	En100 ^c	En100 ^d	En87 (This Study)	En85 ^e	En83 ^f	En82 ^g
V_0 (\AA^3)	832.5(2)	832.9(1)	839(8)	836(3)	833.9(2)	833.12(6)	834.1(5)
K_{70} (GPa)	105.8(5)	109(4)*	104(2)*	103(5)	109(2)	112(1)	115.5(5)
K'_T	8.5(3)	6.6(7)*	10.9(5)*	13(2)	9(1)	7.4(4)	7.82
Method	XRD+BS	XRD+UI	UI	XRD	XRD	XRD	ISLS

^aValues in parentheses indicate the uncertainty in the last significant digit. Errors presented in this study are at the 1σ level. BS: Brillouin spectroscopy; UI: ultrasonic interferometry; ISLS: impulsive stimulated light spectroscopy. (*) indicates adiabatic values: K_{50} is $\sim 1\%$ higher than K_{70} [Angel and Jackson, 2002].

^bAngel and Jackson [2002], $\text{Mg}_2\text{Si}_2\text{O}_6$.

^cKung et al. [2004], $\text{Mg}_2\text{Si}_2\text{O}_6$.

^dFlesch et al. [1998], $\text{Mg}_2\text{Si}_2\text{O}_6$.

^eHugh-Jones and Angel [1997], $(\text{Mg}_{0.85}\text{Fe}_{0.13}\text{Ca}_{0.02})_2(\text{Si}_{0.96}\text{Al}_{0.04})_2\text{O}_6$.

^fHugh-Jones and Angel [1997], $(\text{Mg}_{0.83}\text{Fe}_{0.12}\text{Ca}_{0.006}\text{Al}_{0.04})_2(\text{Si}_{0.97}\text{Al}_{0.03})_2\text{O}_6$.

^gChai et al. [1997], $(\text{Mg}_{1.63}\text{Fe}_{0.17}\text{Ca}_{0.04}\text{Mn}_{0.01})(\text{Al}_{0.12}\text{Cr}_{0.01})(\text{Si}_{1.89}\text{Al}_{0.11})\text{O}_6$.

et al., 2009]. We compare the Debye sound velocity in this study with the calculated values from previous studies on enstatite (Figure 7a). For previous single-crystal studies [Frisillo and Barsch, 1972; Duffy and Vaughan, 1988; Webb and Jackson, 1993; Chai et al., 1997], the Debye sound velocity was determined numerically from averaging the elastic constants using the Christoffel equation [Sturhahn and Jackson, 2007] or from the isotropic V_P and V_S values from experiments on powdered material [Flesch et al., 1998; Kung et al., 2004]. One interesting feature is the decrease of V_D at around 12 GPa, which is observed in our data and Kung et al. [2004]. V_D decreases by about 0.2 km/s when pressure increases from 10.5 to 12.3 GPa. Our in situ XRD pattern shows that there is a transition from the *Pbca* structure to a high-pressure phase, and Mössbauer spectroscopy data show a change in the trend of the hyperfine parameters of En87 [Zhang et al., 2011], so it is reasonable to conclude that the decrease in V_D is related to the structural transition.

[18] By combining the Debye sound velocity determined from NRIXS and the bulk modulus from the P-V equation of state (all determined in this study on En87 from the same bulk sample), it is possible to extract the compressional (V_P) and shear (V_S) sound velocities of En87 as a function of pressure (Figures 7b and 7c). The compressional (V_P) and shear (V_S) sound velocities can be calculated from

$$\frac{3}{V_D^3} = \frac{1}{V_P^3} + \frac{2}{V_S^3} \quad (1)$$

$$\frac{K}{\rho} = V_P^2 - \frac{4}{3}V_S^2 \quad (2)$$

where ρ is the density (corrected for ^{57}Fe enrichment), K is the bulk modulus from the equation of state, and V_D is the Debye sound velocity from the NRIXS measurement. In the calculation, the in situ XRD density and the bulk modulus from the best fit third-order Birch-Murnaghan EOS are used. In this case, we assume that K_{50} can be approximated by K_{70} (K_{50} is $\sim 1\%$ higher than K_{70} [Angel and Jackson, 2002]). The associated uncertainties in determining V_P and V_S from V_D and the bulk modulus have been discussed in detail in Sturhahn and Jackson [2007].

[19] We compare our results with previous studies [Frisillo and Barsch, 1972; Duffy and Vaughan, 1988; Webb and Jackson, 1993; Chai et al., 1997; Flesch et al., 1998; Kung et al., 2004; Jackson et al., 2009] (Figures 7b and 7c). Note that the ambient pressure results of En87 are from NRIXS measurements on a larger aggregate of the sample [Jackson et al., 2009], from which a smaller portion of the sample was drawn for this study. Therefore, the room pressure value of En87 is a very good representation of the average properties of En87 at this pressure. The values of En87 are consistent with a decrease in wave speed with the addition of iron at a given pressure; however, there appears to be an inconsistency in the magnitude of the trend when comparing results from different techniques [Duffy and Vaughan, 1988; Chai et al., 1997; Flesch et al., 1998; Kung et al., 2004; Jackson et al., 2009, 1999]. In the pres-

Table 3. Thermodynamic Parameters of the ^{57}Fe -Participating Vibrations of En87 Determined From NRIXS Spectra at Different Pressures Measured at 300 K^a

Pressure (GPa)	f_{LM}	F_{vib} (meV/atom)	D_{ave} ($\times 10^2$ N/m)	E_k (meV/atom)	c_V (k_B /atom)	S_{vib} (k_B /atom)
0 ^b	0.730(2) ^b	-8.4(3)	1.70(3) ^b , 1.70(3) ^c	14.01(7) ^b	2.75(1) ^b	3.60(1) ^b
3.9(2)	0.755(3)	-3(2)	1.85(27), 1.89(29) ^c	14.2(5)	2.72(5)	3.42(4)
6.9(4)	0.757(3)	-4(3)	1.70(33), 1.68(34) ^c	14.1(6)	2.74(6)	3.45(5)
10.5(7)	0.784(3)	4(2)	2.11(22), 2.31(22) ^c	14.4(4)	2.68(5)	3.19(4)
12.3(7)	0.784(3)	3(2)	2.10(27), 2.10(29) ^c	14.4(5)	2.69(5)	3.22(4)
17(1)	0.797(3)	7(2)	2.20(23), 1.91(24) ^c	14.5(4)	2.67(5)	3.09(4)

^a f_{LM} : Lamb-Mössbauer factor; F_{vib} : free energy; D_{ave} : mean force constant; E_k : kinetic energy; c_V : vibrational specific heat; S_{vib} : vibrational entropy. All parameters were determined from the partial phonon DOS, unless otherwise noted. Uncertainties were determined using the PHOENIX software [Sturhahn, 2000]. Pressures determined from in situ volume measurements of enstatite at 3-ID-B and the BM3 EOS (see text).

^bJackson et al. [2009].

^cDetermined after refinement of the raw data.

Table 4. Thermodynamic Parameters Determined From the DFT-Computed Phonon DOS, Calculated at 0 and 300 K Using PHOENIX^a

DFT phonon DOS	f_{LM}	F_{vib} (meV/atom)	D_{ave} ($\times 10^2$ N/m)	E_k (meV/atom)	c_V (k_B /atom)	S_{vib} (k_B /atom)
Mg ₂ Si ₂ O ₆ total phonon DOS, Figure 5a	NA	89.7, 72.6	10.31, 10.31	14.9, 19.2	0, 2.0	0, 1.7
Fe partial phonon DOS, Figure 5b 25% Fe in the M1-site only	0.94, 0.86	57.5, 31.5	3.51, 3.51	9.4, 15.4	0, 2.5	0, 2.3
Fe partial phonon DOS, Figure 5c 25% Fe in the M2-site only	0.93, 0.83	51.2, 20.4	3.09, 3.09	8.5, 15.1	0, 2.6	0, 2.7

^a f_{LM} : Lamb-Mössbauer factor; F_{vib} : free energy; D_{ave} : mean force constant; E_k : kinetic energy; c_V : vibrational specific heat; S_{vib} : vibrational entropy. NA: not applicable. In the case of the total phonon DOS, the values represent contributions from all atoms in the lattice. For the partial phonon DOS, the values represent contributions from the ⁵⁷Fe-participating vibrations. All parameters are determined using the PHOENIX software at 0 and 300 K, respectively [Sturhahn, 2000].

sure range where we observe OEN (*Pbca*), the V_D , V_P , and V_S increase from room pressure to 10.5 GPa. These trends are consistent with previous measurements in this pressure range [Frisillo and Barsch, 1972; Webb and Jackson, 1993; Chai *et al.*, 1997; Flesch *et al.*, 1998; Kung *et al.*, 2004]. The pressure derivative of the shear modulus for the *Pbca* phase is $d\mu/dP = 1.7 \pm 0.1$ between 0 and 10.5 GPa.

[20] Near the phase transition (10.5 GPa), our in situ XRD pattern at sector 3-ID-B showed that the *Pbca* phase is dominant. A weak $P2_1/c$ ($32\bar{1}$) peak is present at this pressure; however, there is not enough information to resolve its in situ density nor the abundance of the $P2_1/c$ phase. Therefore, we report the sound velocities at 10.5 GPa using the density and bulk modulus from the dominant *Pbca* phase. If one uses the density and bulk modulus of the $P2_1/c$ phase,

the compressional and shear velocities of En87 are within the uncertainties of the *Pbca* phase at 10.5 GPa.

[21] At 12.3 GPa, the (421) peak of the HP phase appears and V_D and V_S for $P2_1/c$ show a drop in velocity (a decrease of ~ 0.2 km/s, $\sim 4\%$ in V_S), rather than a smooth increase (Figure 7). A similar drop in V_S was observed in the Mg end-member using ultrasonic interferometry [Kung *et al.*, 2004]. This behavior is likely related to the structural transition. Interestingly, we do not observe the same decrease in V_P as past studies have reported for the Mg end-member. The V_P value up to 12.3 GPa is similar to the values reported by Chai *et al.* [1997]. In our XRD measurements performed on a sample from the same run charge (Figures 1 and 2), we find that the *Pbca*- $P2_1/c$ structural transition is associated with a volume reduction, which leads to a determined V_P value that shows a slight change in trend near the transition. We show that the Fe atoms are almost entirely in the M2 site, using a combination of Mössbauer spectroscopy, NRIXS, and DFT (Figure 5). Differences in Fe concentration, Fe ordering, and equations of state for the different enstatite samples could, in part, explain the differences in V_P between the studies.

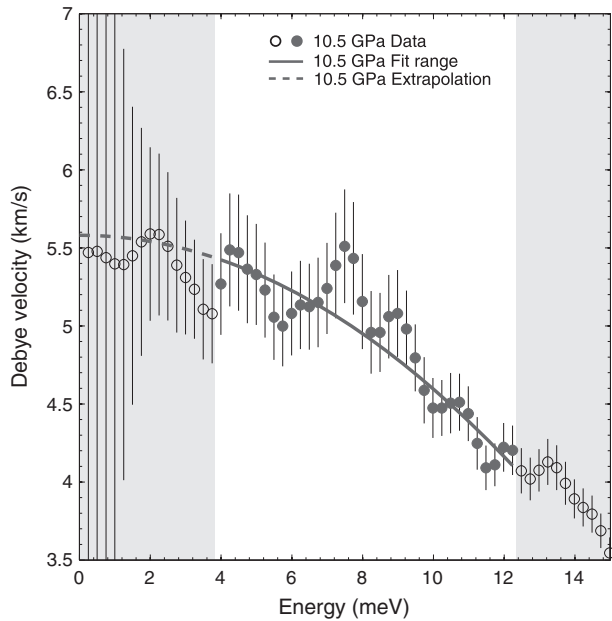


Figure 6. Debye sound velocity (V_D) determination at 10.5 GPa. The fit (solid and dashed lines) was performed on the data (open circles) starting from 3.7 meV (determined by the resolution of the monochromator) and ending at 12.2 meV (determined by chi-square analysis) and then extrapolated to $E = 0$ to determine V_D . Gray regions show the data and associated uncertainties that were not used in the fit.

3.3. Geophysical Implications

[22] Phase transitions of enstatite have been suggested as candidates for the seismic X discontinuity in a depleted mantle [Woodland and Angel, 1997; Woodland, 1998; Kung *et al.*, 2004, 2005; Akashi *et al.*, 2009; Jacobsen *et al.*, 2010]. In seismological studies, the X discontinuity is characterized by a large depth variation, from 240 to 340 km [Deuss and Woodhouse, 2002; Revenaugh and Jordan, 1991; Bagley and Revenaugh, 2008], with reflections associated with a shear impedance increase of 3 to 7.5% (corresponding to a reflection coefficient of 1.5 to 3.8% [Revenaugh and Jordan, 1991; Bagley and Revenaugh, 2008]). The compressional impedance change for this discontinuity is not clear yet. In our study, we identify a transition occurring in enstatite, likely *Pbca*- $P2_1/c$, between 10.1 and 12.2 GPa (a depth equivalent of 300–350 km) accompanied by a shear impedance drop of $\sim 2\%$. The shear impedance of the $P2_1/c$ phase increases by $\sim 8\%$ from 12.3 to 17 GPa. The compressional impedance of enstatite slightly increases by $\sim 2\%$ for the *Pbca*- $P2_1/c$ transition between 10.1 and 12.3 GPa, and it continues to increase by $\sim 7\%$ from 12.3 to 17 GPa. Molecular dynamics simulation [Jahn, 2008] suggests that the $P2_1/c$ phase of the Mg end-member is metastable at high temperature, and multianvil experiments show that the

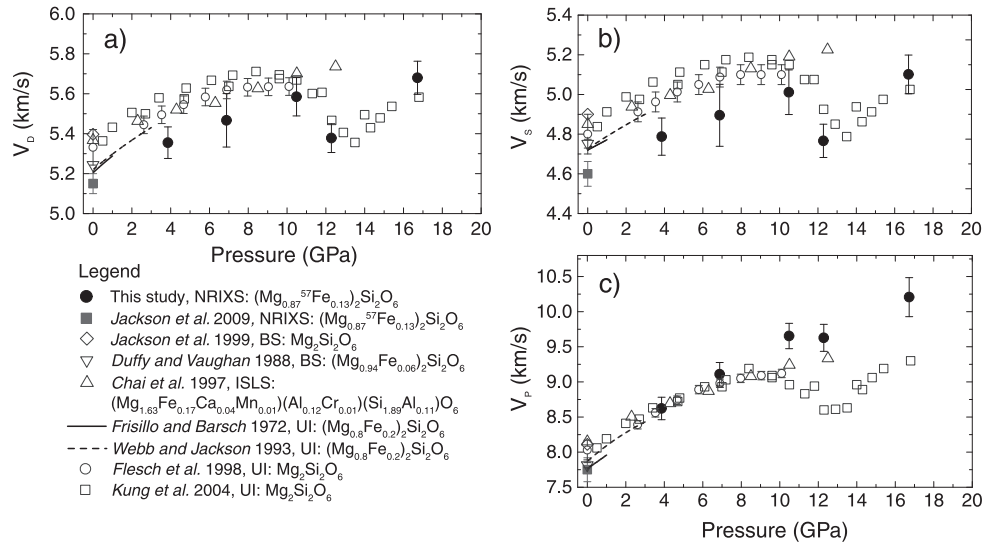


Figure 7. Sound velocities determined from this experiment (see Table 5) and from previous measurements (see Legend). (a) Debye velocity (V_D), (b) shear velocity (V_S), and (c) compressional velocity (V_P). UI: ultrasonic interferometry; BS: Brillouin spectroscopy; ISLS: impulsive stimulated light spectroscopy.

Mg end-member HP-CEN phase is the stable polymorph of enstatite at 14 GPa and 1000°C [Kung *et al.*, 2004]. We explore the influence of iron-bearing *Pbca*-structured enstatite on upper mantle petrologic models, as well as the high-pressure phases of enstatite, and compare these results to seismic observations. Specifically, we focus on the shear properties, as these are well resolved in NRIXS studies (equation 1).

[23] We construct shear velocity profiles for candidate upper mantle assemblages that include *Pbca*-structured enstatite, HP-CEN, and $P2_1/c$ -structured enstatite. We use a finite strain method [Duffy and Anderson, 1989] to primarily assess the influence of *Pbca*-structured enstatite on seismic shear wave structures that have been reported. For the elastic moduli and associated pressure derivatives of enstatite, we use values from this study. We use the thermal expansion coefficient and linear temperature derivatives of the elastic moduli of the *Pbca* phase from Jackson *et al.* [2007]. Thermoelasticity data for olivine ($(\text{Mg}_{0.9}\text{Fe}_{0.1})_2\text{SiO}_4$), $C2/c$ HP-CEN, diopside, and pyrope garnet ($(\text{Mg}_{0.9}\text{Fe}_{0.1})_3\text{Al}_2(\text{SiO}_4)_3$) were taken from recent reports [Wang *et al.*, 1998; Liu *et al.*, 2005; Kung *et al.*, 2005; Isaak *et al.*, 2006; Zou *et al.*, 2012]

(Table 6). We use a 1400°C adiabat in the calculation. Three different petrological models were considered: pyrolite-like with 57% olivine, 14% pyrope garnet, 12% diopside, and 17% enstatite (volume ratio) [Ringwood, 1991]; enstatite-enriched harzburgite with 50% olivine, 10% pyrope garnet, and 40% enstatite [Irifune and Ringwood, 1987; Hieronymus *et al.*, 2007]; and piclogite-like with 16% olivine, 37% pyrope garnet, 23% diopside, 21% jadeite (assume to have the same elastic parameters as diopside), and 3% enstatite [Bass and Anderson, 1984; Ita and Stixrude, 1992] (Figure 8).

[24] We find that the characteristic shear velocities for these three petrological models between 230 and 280 km depths are lower than the global average PREM model [Dziewonski and Anderson, 1981] and higher than the global average AK135 model [Kennett *et al.*, 1995]. It is noteworthy to point out that in this depth region, the average Earth models PREM and AK135 show significantly different wave speeds and gradients (Figure 8). The shear velocities of the petrological models are slightly lower than the shear structure beneath tectonically stable regions such as the eastern North American continent at depths above

Table 5. Elastic Parameters of En87 Determined From This Study Using XRD and NRIXS at Different Pressures^a

Volume (Å ³)	Density (g/cm ³)	Pressure (GPa)	V_D (km/s)	V_P (km/s)	V_S (km/s)	V_Φ (km/s)	$\frac{V_P}{V_S}$	ν	K (GPa)	μ (GPa)
836(3) ^b	3.31(1)	0	5.12(5)	7.7(2)	4.63(5)	5.6(2)	1.669	0.220	103(5)	71(2)
811(2)	3.41(2)	3.9(2)	5.33(8)	8.6(2)	4.78(8)	6.6(2)	1.794	0.274	147(9)	78(2)
795(3)	3.48(3)	6.9(4)	5.5(1)	9.1(2)	4.9(1)	7.1(2)	1.862	0.297	177(9)	83(4)
782(2)	3.54(3)	10.5(7)	5.55(9)	9.6(2)	4.96(9)	7.7(3)	1.935	0.318	210(10)	87(3)
767(3)	3.61(3)	12.3(7)	5.38(7)	9.6(2)	4.79(7)	7.8(3)	2.001	0.332	220(10)	83(2)
752(3)	3.68(3)	17(1)	5.68(8)	10.2(3)	5.05(8)	8.4(5)	2.025	0.339	260(20)	94(3)

^a V_D , V_P , V_S , and V_Φ : Debye, compressional, shear, and bulk sound velocities, respectively; K : bulk modulus; μ : shear modulus. Volume was determined by in situ XRD at APS 3-ID-B (Figure 1b, see text), and density was corrected for ⁵⁷Fe enrichment. Pressures up to 10.5 GPa were determined from the *Pbca* EOS (Table 2), and at 12.3 and 17 GPa, the $P2_1/c$ EOS was used. Error determinations: volume—statistical, density—volume and microprobe uncertainties, K —BM3 fit at the 1 σ level, other parameters—PHOENIX software [Sturhahn, 2000].

^bJackson *et al.* [2009], recalculated V_P , V_S , K , and μ using the *Pbca* EOS from this study.

Table 6. Thermoelastic Parameters of Minerals Used in the Finite Strain Model^a

Minerals	ρ_0 (g/cm ³)	K (GPa)	μ (GPa)	K'	μ'	dK/dT (GPa/K)	$d\mu/dT$ (GPa/K)	α_0 (10 ⁻⁶ K ⁻¹)	α_1 (10 ⁻⁹ K ⁻²)	Reference
OEN	3.31(1) ^b	103(5) ^b	71(2) ^b	13(2) ^b	1.7(1) ^b	-0.0263(3) ^c	-0.0136(3) ^c	29.7 ^c	5.7 ^c	This study ^b <i>Jackson et al. [2007]^c</i>
$P2_1/c$	3.61(3) ^b	220(10) ^b	83(2) ^b	8(4) ^b	2.5(5) ^b	-0.0263(3) ^c	-0.0136(3) ^c	29.7 ^c	5.7 ^c	This study at 12 GPa ^b <i>Jackson et al. [2007]^c</i>
HP-CEN	3.46(1)	156(1)	99(1)	5.6(3)	1.5(1)	-0.017(1)	-0.015(1)	17.3(80)	16.4(11.7)	<i>Kung et al. [2005]</i> at 6.5 GPa
Olivine	3.342(2)	130.3(4)	77.4(2)	4.61(11)	1.61(4)	-0.0164(5)	-0.0130(3)	27.11	6.885	<i>Liu et al. [2005]</i>
Garnet	3.566(1) ^d	170.0(2) ^d	93.2(1) ^d	4.51(2) ^d	1.51(2) ^d	-0.0170(1) ^d	-0.0107(1) ^d	23(2) ^e	9.4(2.8) ^e	<i>Zou et al. [2012]^d</i> <i>Wang et al. [1998]^e</i>
Diopside	3.277(5)	115.9(9)	72.8(4)	4.5(1.8)	1.7	-0.0123	-0.00998	26	10	<i>Isaak et al. [2006]</i>

^aThe DLA (dimensionless logarithmic anharmonic) parameterization [Duffy and Anderson, 1989] was used to compute the shear velocity profiles in Figure 8. The thermal expansion coefficients (α_0 and α_1) were used to correct the densities and pressure derivatives of elastic moduli. For the high-pressure phases ($P2_1/c$ and HP-CEN), the thermoelastic parameters were first projected back to ambient P-T values using the third-order finite strain theory without a temperature correction, and then the projected ambient values were treated the same as the other phases. To compute the velocities of the rock, the average sound velocities were calculated using the Voigt-Reuss-Hill procedure and the Hill average is plotted in Figure 8.

^{b-c}Denotes the associated source reference listed in the last column.

300 km (SNA [Grand and Helmberger, 1984a]). In the same depth range, they are significantly higher (>50 m/s) than the shear velocity structure beneath tectonically active regions such as the western United States (TNA [Grand and Helmberger, 1984a]), the Pacific Ocean (PAC06 [Tan and Helmberger, 2007]), and the northern Atlantic Ocean (ATL [Grand and Helmberger, 1984b]) (Figure 8). The calculated pressure derivative of the shear wave speed (dV_s/dP) is about 0.03 km/s/GPa between 230 and 300 km for these three petrological models. This shear velocity gradient is higher than the average Earth model PREM but lower than regional studies. Based on the phase diagram of enstatite [Woodland, 1998], we assume that the OEN phase ($Pbca$) transitions into the HP-CEN phase ($C2/c$) at 300 km (~ 10 GPa), accompanied by a shear velocity jump [Kung et al., 2005]. It is possible to calculate the shear reflection coefficients, R , for the different petrologies considered here from the shear velocity and density of OEN (this study) and HP-CEN [Kung et al., 2005] using the following equation [Revenaugh and Jordan, 1991; Bagley and Revenaugh, 2008]:

$$R = \frac{\rho_{\text{HP-CEN}} \times V_{\text{HP-CEN}} - \rho_{\text{OEN}} \times V_{\text{OEN}}}{\rho_{\text{HP-CEN}} \times V_{\text{HP-CEN}} + \rho_{\text{OEN}} \times V_{\text{OEN}}} \quad (3)$$

[25] The shear reflection coefficients corresponding to different petrological compositions are 0.5% (pyrolite), 1.2% (enstatite-enriched harzburgite), and 0.1% (piclogite) at 300 km depth. The calculated shear reflection coefficients are lower than seismic observations for the “X discontinuity” (1.5 to 3.5%) [Revenaugh and Jordan, 1991; Bagley and Revenaugh, 2008]. Based on our XRD and NRIXS data, we also compute the shear velocity profile of the pyrolytic mantle, speculating that the $Pbca$ phase gradually transitions into the $P2_1/c$ phase from 10 to 12 GPa (Figure 8). We note that the existence of the $P2_1/c$ phase in the mantle remains speculative.

[26] Although iron-bearing enstatite-rich phase assemblages may produce lower than average shear velocities, it appears that between 250 and 300 km depths in tectonically active regions, changes in candidate petrologic assemblages (i.e., pyrolite, piclogite, and harzburgite) may not be enough to explain the very low shear velocities observed. Partial melting [Tan and Helmberger, 2007] or a hydrated phase

assemblage may help explain the nonpervasive distribution of the X discontinuity [Jacobsen et al., 2010; Revenaugh and Jordan, 1991]. However, observations of the X discontinuity in regions expected to be dry, such as the underside region

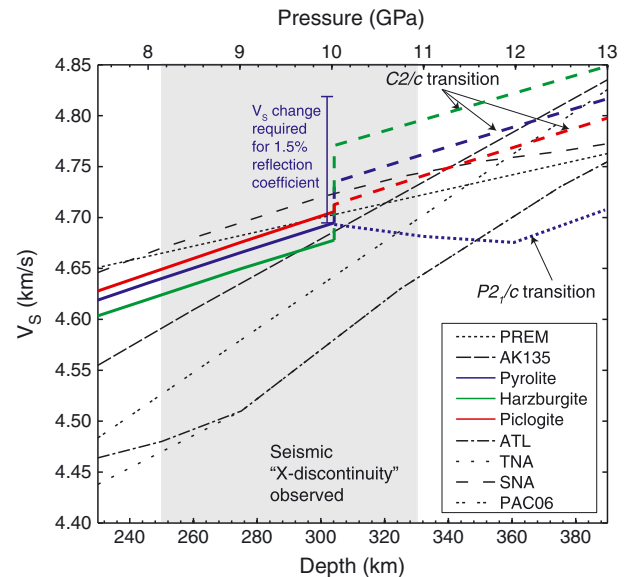


Figure 8. Comparison of calculated shear wave velocities from candidate upper mantle petrological models (1400°C adiabat; see text) with seismic profiles. At $P > 10$ GPa: assuming $C2/c$ transition (dashed curve) [Kung et al., 2005]; speculating that the $P2_1/c$ transition occurs (dotted curve) (this study). See text for details. Seismic X discontinuity observed (shaded region) [Revenaugh and Jordan, 1991; Bagley and Revenaugh, 2008]. Global seismic models: PREM (230–390 km in depth, 7.5–13.0 GPa in pressure, interpolated between reported values) [Dziewonski and Anderson, 1981] and AK135 [Kennett et al., 1995]. Regional seismic models: SNA [Grand and Helmberger, 1984a], TNA [Grand and Helmberger, 1984a], ATL [Grand and Helmberger, 1984b], and PAC06 (interpolated between reported values) [Tan and Helmberger, 2007]. Shear velocity jump required for a seismic reflection with 1.5% reflection coefficient in a pyrolytic mantle (blue scale at 300 km) [Bagley and Revenaugh, 2008].

of subducted slabs, will likely require alternative explanations than those considered here. Nevertheless, we find that phase assemblages containing considerable fractions of *Pbca*-structured iron-bearing enstatite can produce shear velocities that are lower than what is observed under stable tectonic regions (SNA [Grand and Helmberger, 1984a]) and the 1-D Earth model PREM.

[27] In this manuscript, we report the high-pressure elasticity of the ^{57}Fe -enriched En87 sample constrained by X-ray diffraction and nuclear resonant inelastic X-ray scattering experiments up to 19.1 GPa. A BM3 EOS fitting gives $K_{T0} = 103 \pm 5$ GPa and $K'_{T0} = 13 \pm 2$ for the *Pbca* phase. At 12 GPa, a BM3 EOS fitting gives $K_{T12} = 220 \pm 10$ GPa with $K'_{T12} = 8 \pm 4$ for the $P2_1/c$ phase. A structural transition from the *Pbca* phase to the $P2_1/c$ phase is observed between 10.1 and 12.2 GPa, associated with a shear velocity decrease by $\sim 4\%$. DFT calculations of the partial phonon DOS of enstatite are consistent with Fe^{2+} dominantly occupying the M2 site, consistent with experimental constraints on the iron occupancy of our sample. By using the shear velocity determined from this study and a finite strain model, we compute shear velocity profiles for different upper mantle petrological compositions. The shear velocity jump associated with the *Pbca*- $C2/c$ transition has a shear reflection coefficient lower than that observed for the seismic “X discontinuity.” The low velocities reported in tectonically active regions are unlikely to be explained by the presence of enstatite alone and may require phase assemblages containing hydrous phases and/or partial melt. We find that candidate upper mantle phase assemblages containing *Pbca*-structured enstatite are associated with shear velocity gradients that are higher than the average Earth model PREM but lower than regional studies down to about 250 km depth.

[28] **Acknowledgments.** We thank C. A. Murphy, J. K. Wicks, and A. S. Wolf for help in conducting experiments and Y. Fei for synthesizing the sample. We thank the NSF (CAREER EAR-0956166) and the Tectonics Observatory at Caltech (funded through the Gordon and Betty Moore Foundation) for support of this research. Use of the Advanced Photon Source was supported by the U.S. D.O.E., O.S., and O.B.E.S. (DE-AC02-06CH11357). Use of the Advanced Light Source was supported by the U.S. D.O.E., O.S., and O.B.E.S. (DE-AC02-05CH11231). Sector 3 operations, the gas-loading system at GSECARS, and beamline 12.2.2 are supported in part by COMPRES under NSF Cooperative Agreement EAR 06-49658.

References

Akashi, A., Y. Nishihara, E. Takahashi, Y. Nakajima, Y. Tange, and K. Funakoshi (2009), Orthoenstatite/clinoenstatite phase transformation in MgSiO_3 at high pressure and high temperature determined by in situ X-ray diffraction: Implications for nature of the X-discontinuity, *J. Geophys. Res.*, *114*, B04206, doi:10.1029/2008JB005894.

Angel, R. J. (2000), Equations of state, in *High-Temperature and High-Pressure Crystal Chemistry, Reviews in Mineralogy and Geochemistry*, vol. 41, edited by R. M. Hazen and R. T. Downs, pp. 35–59, Mineral. Soc. Am., Washington, D. C.

Angel, R. J., and D. A. Hugh-Jones (1994), Equations of state and thermodynamic properties of enstatite pyroxenes, *J. Geophys. Res.*, *99*(B10), 19,777–19,783.

Angel, R. J., and J. M. Jackson (2002), Elasticity and equation of state of orthoenstatite, MgSiO_3 , *Am. Mineral.*, *87*(4), 558–561.

Bagley, B., and J. Revenaugh (2008), Upper mantle seismic shear discontinuities of the Pacific, *J. Geophys. Res.*, *113*, B12301, doi:10.1029/2008JB005692.

Baroni, S., P. Giannozzi, and A. Testa (1987), Green's-function approach to linear response in solids, *Phys. Rev. Lett.*, *58*(18), 1861–1864.

Baroni, S., S. de Gironcoli, A. Dal Corso, and P. Giannozzi (2001), Phonons and related crystal properties from density-functional perturbation theory, *Rev. Modern Phys.*, *73*(2), 515–562.

Bass, J. D., and D. L. Anderson (1984), Composition of the upper mantle: Geophysical tests of two petrological models, *Geophys. Res. Lett.*, *11*(3), 237–240.

Boehler, R. (2000), High-pressure experiments and the phase diagram of lower mantle and core materials, *Rev. Geophys.*, *38*(2), 221–245.

Caracas, R., and X. Gonze (2010), Lattice dynamics and thermodynamical properties, in *Thermodynamic Properties of Solids: Experiment and Modeling*, edited by S. L. Chaplot et al., pp. 291–315, Wiley-VCH Verlag, Weinheim.

Chai, M., J. M. Brown, and L. J. Slutsky (1997), The elastic constants of an aluminous orthopyroxene to 12.5 GPa, *J. Geophys. Res.*, *102*(B7), 14,779–14,785.

Chu, R., B. Schmandt, and D. V. Helmberger (2011), Juan de Fuca subduction zone from a mixture of tomography and waveform modeling, *J. Geophys. Res.*, *117*, B03304, doi:10.1029/2012JB009146.

Chu, R., B. Schmandt, and D. V. Helmberger (2012), Upper mantle P velocity structure beneath the Midwestern United States derived from triplicated waveforms, *Geochem. Geophys. Geosy.*, *13*, Q0AK04, doi:10.1029/2011GC003818.

Deuss, A., and J. H. Woodhouse (2002), A systematic search for mantle discontinuities using SS-precursors, *Geophys. Res. Lett.*, *29*(8), 1249–1252, doi:10.1029/2002GL014768.

Dewaele, A., F. Datchi, P. Loubeyre, and M. Mezouar (2008), High pressure-high temperature equations of state of neon and diamond, *Phys. Rev. B*, *77*(9), 094106.

Duffy, T. S., and D. L. Anderson (1989), Seismic velocities in mantle minerals and the mineralogy of the upper mantle, *J. Geophys. Res.*, *94*(B2), 1895–1912.

Duffy, T. S., and M. T. Vaughan (1988), Elasticity of enstatite and its relationship to crystal-structure, *J. Geophys. Res.*, *93*(B1), 383–391.

Dziewonski, A. M., and D. L. Anderson (1981), Preliminary reference Earth model, *Phys. Earth. Planet. In.*, *25*, 297–356.

Flesch, L. M., B. S. Li, and R. C. Liebermann (1998), Sound velocities of polycrystalline MgSiO_3 -orthopyroxene to 10 GPa at room temperature, *Am. Mineral.*, *83*(5-6), 444–450.

Frisillo, A. L., and G. R. Barsch (1972), Measurement of single-crystal elastic-constants of bronzite as a function of pressure and temperature, *J. Geophys. Res.*, *77*(32), 6360–6384.

Frost, D. J. (2008), The upper mantle and transition zone, *Elements*, *4*, 171–176.

Fuchs, M., and M. Scheffler (1999), Ab initio pseudopotentials for electronic structure calculations of poly-atomic systems using density-functional theory, *Comput. Phys. Commun.*, *119*(1), 67–98.

Gonze, X., and J. P. Vigneron (1989), Density-functional approach to nonlinear-response coefficients of solids, *Phys. Rev. B*, *39*(18), 13,120–13,128.

Gonze, X., D. C. Allan, and M. P. Teter (1992), Dielectric tensor, effective charges, and phonons in α -quartz by variational density-functional perturbation theory, *Phys. Rev. Lett.*, *68*(24), 3603–3606.

Gonze, X., G. M. Rignanese, and R. Caracas (2005), First-principles studies of the lattice dynamics of crystals, and related properties, *Zeitschrift Kristallogr.*, *220*(5-6), 458–472.

Grand, S. P., and D. V. Helmberger (1984a), Upper mantle shear structure of North America, *Geophys. J. Roy. Astr. Soc.*, *76*, 399–438.

Grand, S. P., and D. V. Helmberger (1984b), Upper mantle shear structure beneath the northwest Atlantic Ocean, *J. Geophys. Res.*, *89*(B13), 11,465–11,475.

Hammersley, A. P., S. O. Svensson, M. Hanfland, A. N. Fitch, and D. Hausermann (1996), Two-dimensional detector software: From real detector to idealised image or two-theta scan, *High Pressure Res.*, *14*(4-6), 235–248.

Henke, B. L., E. M. Gullikson, and J. C. Davis (1993), X-ray interactions: Photoabsorption, scattering, transmission, and reflection at $e = 50$ –30,000 eV, $z = 1$ –92, *Atom. Data Nucl. Data.*, *54*(2), 181–342.

Hieronymus, C. F., Z. H. Shomali, and L. B. Pedersen (2007), A dynamical model for generating sharp seismic velocity contrasts underneath continents: Application to the Sorgenfrei-Tornquist Zone, *Earth. Planet. Sci. Lett.*, *262*, 77–91.

Hohenberg, P., and W. Kohn (1964), Inhomogeneous electron gas, *Phys. Rev.*, *136*(3B), B864–B871.

Holland, T. J. B., and S. A. T. Redfern (1997), Unit cell refinement from powder diffraction data: The use of regression diagnostics, *Mineral. Mag.*, *61*(1), 65–77.

Hugh-Jones, D. A., and R. J. Angel (1994), A compressional study of MgSiO_3 orthoenstatite up to 8.5-GPa, *Am. Mineral.*, *79*(5-6), 405–410.

Hugh-Jones, D. A., and R. J. Angel (1997), Effect of Ca^{2+} and Fe^{2+} on the equation of state of MgSiO_3 orthopyroxene, *J. Geophys. Res.*, *102*(B6), 12,333–12,340.

- Irifune, T., and A. E. Ringwood (1987), Phase transformations in a harzburgite composition to 26 GPa: Implications for dynamical behaviour of the subducting slab, *Earth. Planet. Sci. Lett.*, *86*(2-4), 365–376.
- Isaak, D. G., I. Ohno, and P. C. Lee (2006), The elastic constants of monoclinic single-crystal chrome-diopside to 1,300 K, *Phys. Chem. Miner.*, *32*, 691–699.
- Ita, J., and L. Stixrude (1992), Petrology, elasticity, and composition of the mantle transition zone, *J. Geophys. Res.*, *97*(B5), 6849–6866.
- Jackson, J. M., S. V. Sinogeikin, and J. D. Bass (1999), Elasticity of MgSiO₃ orthoenstatite, *Am. Mineral.*, *84*(4), 677–680.
- Jackson, J. M., S. V. Sinogeikin, M. A. Carpenter, and J. D. Bass (2004), Novel phase transition in orthoenstatite, *Am. Mineral.*, *89*, 239–244.
- Jackson, J. M., S. V. Sinogeikin, and J. D. Bass (2007), Sound velocities and single-crystal elasticity of orthoenstatite to 1073 K at ambient pressure, *Phys. Earth. Planet. In.*, *161*, 1–12.
- Jackson, J. M., E. A. Hamecher, and W. Sturhahn (2009), Nuclear resonant X-ray spectroscopy of (Mg,Fe)SiO₃ orthoenstatites, *Eur. J. Mineral.*, *21*, 551–560.
- Jacobsen, S. D., Z. X. Liu, T. B. Ballaran, E. F. Littlefield, L. Ehm, and R. J. Hemley (2010), Effect of H₂O on upper mantle phase transitions in MgSiO₃: Is the depth of the seismic X-discontinuity an indicator of mantle water content? *Phys. Earth. Planet. In.*, *183*, 234–244.
- Jahn, S. (2008), High-pressure phase transitions in MgSiO₃ orthoenstatite studied by atomistic computer simulation, *Am. Mineral.*, *93*, 528–532.
- Kennett, B. L. N., E. R. Engdahl, and R. Buland (1995), Constraints on seismic velocities in the Earth from traveltimes, *Geophys. J. Int.*, *122*(1), 108–124.
- Kohn, W., and L. J. Sham (1965), Self-consistent equations including exchange and correlation effects, *Phys. Rev.*, *140*(4A), A1133–A1138.
- Kung, J., B. Li, T. Uchida, Y. Wang, D. Neuville, and R. C. Liebermann (2004), In situ measurements of sound velocities and densities across the orthopyroxene high-pressure clinopyroxene transition in MgSiO₃ at high pressure, *Phys. Earth. Planet. In.*, *147*, 27–44.
- Kung, J., B. Li, T. Uchida, and Y. Wang (2005), In-situ elasticity measurement for the unquenchable high-pressure clinopyroxene phase: Implication for the upper mantle, *Geophys. Res. Lett.*, *32*(1), L01307, doi:10.1029/2005GL024904.
- LeFevre, L. V., and D. V. Helmberger (1989), Upper mantle P velocity structure of the Canadian shield, *J. Geophys. Res.*, *94*(B12), 17,749–17,765.
- Liu, W., J. Kung, and B. Li (2005), Elasticity of San Carlos olivine to 8 GPa and 1073 K, *Geophys. Res. Lett.*, *32*(16), L16301, doi:10.1029/2005GL023453.
- Mao, H. K., J. Xu, and P. M. Bell (1986), Calibration of the ruby pressure gauge to 800-kbar under quasi-hydrostatic conditions, *J. Geophys. Res.*, *91*(B5), 4673–4676.
- Monkhorst, H. J., and J. D. Pack (1976), Special points for Brillouin-zone integrations, *Phys. Rev. B*, *13*(12), 5188–5192.
- Perdew, J. P., K. Burke, and M. Ernzerhof (1996), Generalized gradient approximation made simple, *Phys. Rev. Lett.*, *77*, 3865–3868.
- Revenaugh, J., and T. H. Jordan (1991), Mantle layering from ScS reverberations. 3. The upper mantle, *J. Geophys. Res.*, *96*(B12), 19,781–19,810.
- Ringwood, A. E. (1991), Phase transformations and their bearing on the constitution and dynamics of the mantle, *Geochim. Cosmochim. Ac.*, *55*(8), 2083–2110.
- Rivers, M., V. B. Prakapenka, A. Kubo, C. Pullins, C. M. Holl, and S. D. Jacobsen (2008), The COMPRES/GSECARS gas-loading system for diamond anvil cells at the Advanced Photon Source, *High Pressure Res.*, *28*, 273–292.
- Schauble, E. A. (2004), Applying stable isotope fractionation theory to new systems, *Rev. Mineral. Geochem.*, *55*, 65–111.
- Shimizu, H., H. Imaeda, T. Kume, and S. Sasaki (2005), High-pressure elastic properties of liquid and solid neon to 7 GPa, *Phys. Rev. B*, *71*, 014,108–014,112.
- Shinmei, T., N. Tomioka, K. Fujino, K. Kuroda, and T. Irifune (1999), In situ X-ray diffraction study of enstatite up to 12 GPa and 1473 K and equations of state, *Am. Mineral.*, *84*(10), 1588–1594.
- Sturhahn, W. (2000), CONUSS and PHOENIX: Evaluation of nuclear resonant scattering data, *Hyperfine Interact.*, *125*(1-4), 149–172.
- Sturhahn, W. (2004), Nuclear resonant spectroscopy, *J. Phys.-Condens. Mat.*, *16*, S497–S530.
- Sturhahn, W., and J. M. Jackson (2007), Geophysical applications of nuclear resonant spectroscopy, in *Advances in High-Pressure Mineralogy: Geological Society of America Special Paper 421*, edited by E. Ohtani, pp. 157–174, Geological Society of America, Inc., Boulder, Colo., doi:10.1130/2007.2421(09).
- Tan, Y., and D. V. Helmberger (2007), Trans-Pacific upper mantle shear velocity structure, *J. Geophys. Res.*, *112*, B08301.
- Toellner, T. S. (2000), Monochromatization of synchrotron radiation for nuclear resonant scattering experiments, *Hyperfine Interact.*, *125*(1-4), 3–28.
- Troullier, N., and J. Martins (1991), Efficient pseudopotentials for plane-wave calculations, *Phys. Rev. B*, *43*, 1993–2006.
- Wang, Y., D. J. Weidner, J. Zhang, G. D. Gwanmesia, and R. C. Liebermann (1998), Thermal equation of state of garnets along the pyrope-majorite join, *Phys. Earth. Planet. In.*, *105*(1-2), 59–71.
- Webb, S. L., and I. Jackson (1993), The pressure-dependence of the elastic-moduli of single-crystal ortho-pyroxene (Mg_{0.8}Fe_{0.2})SiO₃, *Eur. J. Mineral.*, *5*(6), 1111–1119.
- Weidner, D. J., H. Wang, and J. Ito (1978), Elasticity of orthoenstatite, *Phys. Earth. Planet. In.*, *17*(2), 7–13.
- Woodland, A. B. (1998), The orthorhombic to high-P monoclinic phase transition in Mg-Fe pyroxenes: Can it produce a seismic discontinuity? *Geophys. Res. Lett.*, *25*(8), 1241–1244.
- Woodland, A. B., and R. J. Angel (1997), Reversal of the orthoferrosilite-high-P clinoferrosilite transition, a phase diagram for FeSiO₃ and implications for the mineralogy of the Earth's upper mantle, *Eur. J. Mineral.*, *9*(2), 245–254.
- Zhang, D., J. M. Jackson, W. Sturhahn, and Y. Xiao (2011), Local structure variations observed in orthoenstatite at high pressures, *Am. Mineral.*, *96*, 1585–1592.
- Zhang, J. S., P. Dera, and J. D. Bass (2012), A new high-pressure phase transition in natural Fe-bearing orthoenstatite, *Am. Mineral.*, *97*(7), 1070–1074.
- Zhao, J. Y., W. Sturhahn, J. F. Lin, G. Y. Shen, E. E. Alp, and H. K. Mao (2004), Nuclear resonant scattering at high pressure and high temperature, *High Pressure Res.*, *24*, 447–457.
- Zou, Y., T. Irifune, G. Steeve, M. L. Whitaker, T. Shinmei, H. Ohfuji, R. Negishi, and Y. Higo (2012), Elasticity and sound velocities of polycrystalline Mg₃Al₂(SiO₄)₃ garnet up to 20 GPa and 1700 K, *J. Applied Phys.*, *112*, 014910, doi:10.1063/1.4736407.